coatings

MDPI

Article

Theoretical and Numerical Constant Mean Curvature Surface and Liquid Entry Pressure Calculations for a Combined Pillar–Pore Structure

Tobias Jäger [1,*], Jemp Keup [1], Nikolaos I. Prasianakis [2] and Stephan Leyer [1]

[1] Department of Engineering, Faculty of Science, Technology and Medicine, University of Luxembourg, L-1359 Luxembourg, Luxembourg; stephan.leyer@uni.lu (S.L.)
[2] Transport Mechanisms Group, Laboratory for Waste Management, Paul Scherrer Institute, 5232 Villigen, Switzerland; nikolaos.prasianakis@psi.ch
* Correspondence: tobias.jaeger@uni.lu; Tel.: +352-466-644-9621

Abstract: Modern microfabrication techniques have led to a growing interest in micropillars and pillar–pore structures. Therefore, in this paper a study of the liquid entry pressure of a hydrophobic pillar–pore structure and the corresponding liquid–gas interface shape for the pressurized liquid is presented. We theoretically analysed the constant mean curvature problem for the rotationally symmetric case and determined an analytical expression for the liquid entry pressure of a hydrophobic pillar–pore structure. Furthermore, the shape of the liquid–gas interface as well as a formula for the location of the minimum were derived. The results are useful for designing geometries with specific properties, such as preventing or facilitating liquid intrusion into rough structures. We compared these results to multiphase lattice Boltzmann simulations where equilibrium contact angles in the range of 157° to 102° were tested. In our further analysis, we compared theoretical findings from previous works to our lattice Boltzmann simulations. The presented cases can serve as a benchmark for the development and validation of numerical multiphase models.

Keywords: lattice Boltzmann method; multiphase flow; liquid entry pressure; constant mean curvature surface; pillar; pore; interface shape

Citation: Jäger, T.; Keup, J.; Prasianakis, N.I.; Leyer, S. Theoretical and Numerical Constant Mean Curvature Surface and Liquid Entry Pressure Calculations for a Combined Pillar–Pore Structure. *Coatings* **2023**, *13*, 865. https://doi.org/10.3390/coatings13050865

Academic Editor: Emerson Coy

Received: 14 March 2023
Revised: 17 April 2023
Accepted: 27 April 2023
Published: 3 May 2023

1. Introduction

Materials with hydrophobic surfaces are of interest for many industrial applications. Recently, there has been a great deal of interest in so-called superhydrophobic surfaces, which are created by a combination of chemical treatment and local roughness to increase hydrophobicity, i.e., to reduce the wettability of a surface. Microfabrication techniques have made it possible to produce a variety of artificial superhydrophobic surfaces with precisely controlled local roughness on the micrometer scale [1–3]. In addition, membrane treatments such as micropillars and hydrophobic coatings can reduce scaling and extend the lifetime of a membrane [3]. Following Agonafer et al. [4], the ability to manipulate fluid interfaces, such as retaining fluid behind or within porous structures, is useful in numerous applications, including microfluidics and biochemical analysis. In their work they fabricated customized pillar–pore structures at micrometer scale and analysed the wetting behaviour. Many applications, such as oil transportation [5], water/oil separation [6,7], and thermal management of micro/power electronic systems [8], call for porous structures with the ability to retain low-surface-tension liquids (such as dielectric refrigerants and oils) against an imposed pressure difference [4].

Among other properties, hydrophobic porous membranes are characterised by their liquid entry pressure (LEP). The LEP is the pressure difference that needs to be applied to a dry membrane in order to force the liquid to penetrate the interior of the membrane. For structures such as a cylindrical or a torus–shaped pore, analytical expressions for the LEP have been derived [9,10].

The shape of the liquid–gas interface for a pressurized liquid on top of a hydrophobic structure is governed by the Young–Laplace equation, which describes the capillary pressure difference sustained across the interface between two static fluids. The three–phase gas–liquid–solid contact line is assumed to be attached to the outer edge of the hydrophobic structure [11]. The most general form of the Young—Laplace equation is given by [9,12]:

$$\Delta p = \gamma \operatorname{div} \hat{\mathbf{n}} = 2\gamma H_f = \gamma \left(\frac{1}{R_1} + \frac{1}{R_2} \right) \tag{1}$$

Here γ is the surface tension, $\operatorname{div} \hat{\mathbf{n}}$ is the divergence of the unit normal vector of the liquid–gas interface, H_f is the mean curvature, and R_1 and R_2 are the principal radii of curvature at a given point on the liquid–gas interface.

For a static situation without body forces such as, e.g., gravity, the pressure within each fluid phase is constant, leading to a surface of constant mean curvature (CMC) [11]. This also means that Δp is constant at every point of the liquid–gas interface. It follows directly that solely $q := \Delta p / \gamma$ and the boundary condition, in the form of the three-phase gas–liquid–solid contact line, define the shape of the liquid–gas interface.

The LEP for a cylindrical pore is the pressure difference that is required for water to enter a hydrophobic cylindrical pore and wet the pore wall. For a perfect cylindrical pore with a radius (r_c), the LEP can be calculated using the following formula [9,10,13]:

$$\mathrm{LEP} = \frac{-2\gamma \cos \alpha_0}{r_c} \tag{2}$$

Thereby α_0 is the equilibrium contact angle of a water droplet on a flat surface of the pore material. The equilibrium contact angle α_0 increases with increasing hydrophobicity. The magnitude of the contact angle can be calculated using Young's equation [14]. A material is considered hydrophobic if the equilibrium contact angle is bigger than 90°. More details regarding equilibrium contact angle determination can be found, e.g., in [15–17].

For a vanishing pressure difference, the liquid–gas interface is flat. Applying a pressure difference leads to a spherical meniscus with radius r_m (see Figure 1). As the pressure difference increases, r_m shrinks. This results in an increase in the contact angle until it reaches the critical value of α_0. At this point, the hydrophobic material can no longer prevent the intrusion of water. The corresponding formula for this LEP can be derived directly from the Young–Laplace Equation (1) with $R_1 = R_2 = r_m$ and by using the trigonometric relation $-\cos \alpha = r_c / r_m$. Equation (2) is only correct if the pressure in the meniscus is constant and gravitational effects are negligible. In [18], we showed that a multiphase LB method can correctly predict the LEP pressure for a cylindrical pore.

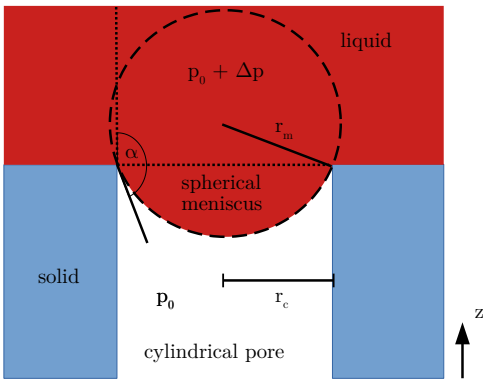

Figure 1. Side view of a cylindrical pore with spherical meniscus.

Zheng et al. [19] showed that the critical pressure difference Δp_{crit} to enter a structure decorated with periodic micropillars can be calculated with the following force balance approach:

$$\Delta p_{crit}(A_c - A) = -\gamma l \cos(\alpha_0) \quad (3)$$

A_c is the area of the periodically repeated cell, l is the perimeter of the pillar, and A is the pillar cross-sectional area. In this work we focus on the special case of round pillars with radius r_p. Therefore, $A_c = P \times P$, $A = \pi r_p^2$, and $l = 2\pi r_p$ (see Figure 2).

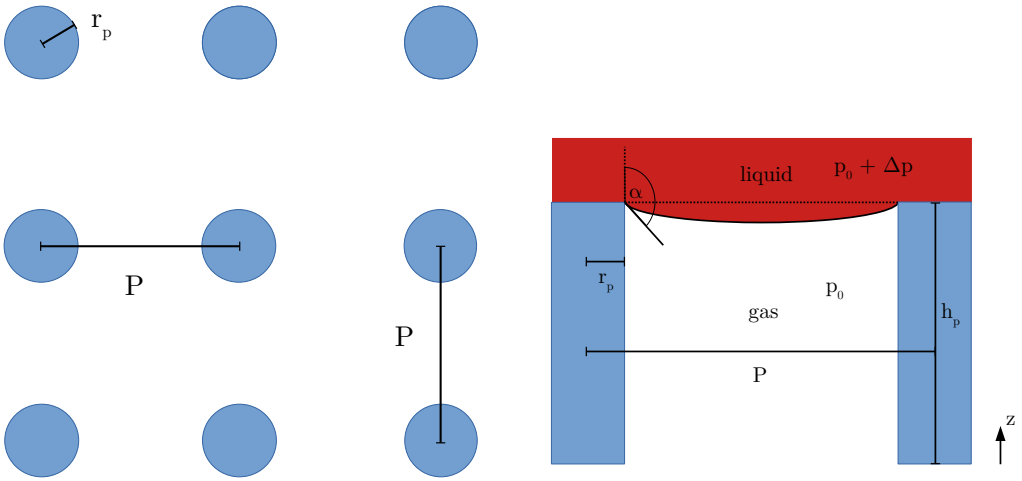

(**a**) (**b**)

Figure 2. Top view (**a**) and side view (**b**) for a periodically repeated pillar structure.

Zheng et al. [19] have addressed the issue of interfacial deformation by using a finite element method to calculate the shape of the liquid–gas interface for a statically pressurized liquid in contact with a superhydrophobic surface. Zheng et al. [19] found good agreement of Equation (3) with the predictions of the finite element method (FEM). Lobaton and Salamon [11] numerically solved a Lagrangian evolution problem to obtain the surface of constant mean curvature for a given pressure difference. In [18] we showed that a multiphase lattice Boltzmann method can also be used to determine the shape of the static liquid–gas interface.

In this work we determine an analytical expression for the LEP of a combined pillar–pore structure. This is the critical pressure difference Δp_{crit} sustained across the liquid–gas interface at which the liquid begins to enter a cylindrical pore with a cylindrical pillar in the centre of the pore (see Figure 3). We also provide a theoretical analysis of the liquid–gas interface shape and compare the theoretical findings with multiphase lattice Boltzmann simulation results. A deeper understanding of the interface shape for this specific pillar–pore structure can be useful for designing surfaces with specific properties, such as preventing or facilitating liquid intrusion. Here we assume that the pillar and the pore wall have the same surface properties, which leads to an identical equilibrium contact angle.

We also compare the critical pressure difference Δp_{crit} to numerical results obtained with the lattice Boltzmann (LB) method. Furthermore, we compare the predictions of Equation (3) from Zheng et al. [19] to numerical results obtained with the LB method.

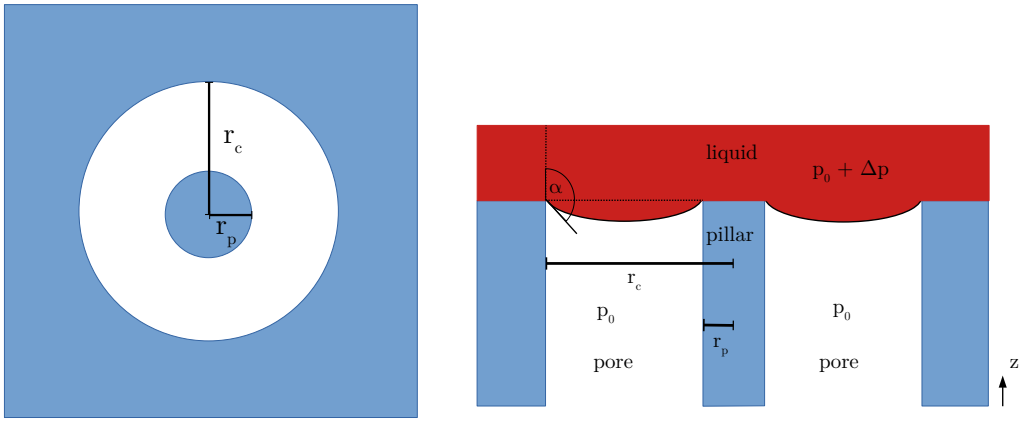

(**a**) (**b**)

Figure 3. Top view (**a**) and side view (**b**) for a combined pillar–pore structure. Here r_c is the radius of the cylindrical pore and r_p is the radius of the cylindrical pillar.

2. Mathematical Background

The relationship $g(x,y,z) = f(x,y) - z = 0$ defines a surface, and $\mathbf{n} = \nabla g(x,y,z)$ is a vector normal to this surface. With the norm $|\mathbf{n}| = \sqrt{1 + (\partial_x f(x,y))^2 + (\partial_y f(x,y))^2}$, one obtains the unit normal vector $\hat{\mathbf{n}} = \mathbf{n}/|\mathbf{n}|$. Inserting this into the Young–Laplace Equation (1), one obtains a partial differential equation (PDE) in Cartesian coordinates

$$\partial_x \left(\frac{f(x,y)}{\sqrt{1 + (\partial_x f(x,y))^2 + (\partial_y f(x,y))^2}} \right) + \partial_y \left(\frac{f(x,y)}{\sqrt{1 + (\partial_x f(x,y))^2 + (\partial_y f(x,y))^2}} \right) = -\frac{\Delta p}{\gamma} \quad (4)$$

for a surface of arbitrary shape, as stated, e.g., in [19].

In the case of a combined pillar–pore structure, cylindrical coordinates (r, φ, z) are appropriate to describe the problem. Therefore, we use the corresponding divergence div and gradient ∇.

$$\operatorname{div} \hat{\mathbf{n}} = \frac{1}{r}\frac{\partial}{\partial r}(r\hat{n}_r) + \frac{1}{r}\frac{\partial \hat{n}_\varphi}{\partial \varphi} + \frac{\partial \hat{n}_z}{\partial z} \quad (5)$$

$$\nabla g(r,\varphi,z) = \frac{\partial g}{\partial r}\hat{\mathbf{e}}_r + \frac{1}{r}\frac{\partial g}{\partial \varphi}\hat{\mathbf{e}}_\varphi + \frac{\partial g}{\partial z}\hat{\mathbf{e}}_z \quad (6)$$

Analogous to the expression in Cartesian coordinates, $g(r,\varphi,z) = f(r,\varphi) - z = 0$ defines a surface in cylindrical coordinates and $\mathbf{n} = \nabla g(r,\varphi,z)$ is a vector normal to the surface. For the special case of a rotationally symmetric solution, the definition of the surface simplifies to:

$$g(r,z) = f(r) - z = 0 \quad (7)$$

The normal vector $\mathbf{n}$ can be found with the gradient:

$$\mathbf{n} = \nabla g(r,z) = \frac{\partial f(r)}{\partial r}\hat{\mathbf{e}}_r - \hat{\mathbf{e}}_z \quad (8)$$

$$|\mathbf{n}| = \left(1 + \left(\frac{\partial f(r)}{\partial r}\right)^2\right)^{\frac{1}{2}} \quad (9)$$

The norm $|\mathbf{n}|$ can be used to derive the unit normal vector $\hat{\mathbf{n}}$:

$$\hat{\mathbf{n}} = \frac{\mathbf{n}}{|\mathbf{n}|} = \underbrace{\frac{\partial f(r)}{\partial r}\left(1+\left(\frac{\partial f(r)}{\partial r}\right)^2\right)^{-\frac{1}{2}}}_{\hat{n}_r}\hat{\mathbf{e}}_r \underbrace{-\left(1+\left(\frac{\partial f(r)}{\partial r}\right)^2\right)^{-\frac{1}{2}}}_{\hat{n}_z}\hat{\mathbf{e}}_z \tag{10}$$

3. Numerical Methods

To capture the interface shape of a liquid under pressure, one can solve the PDE (4) numerically, e.g., with the FEM, as done by Zheng et al. [19]. Lobaton and Salamon [11] used a different approach and solved a Lagrangian evolution problem to obtain the static interface shape. Both methods assume a fixed three-phase contact line or a fixed contact angle attached to the hydrophobic solid structure, which then serves as a static boundary condition for the PDE. To overcome this limitation, one can use a multiphase model that includes fluid–solid interaction. Such a model makes it possible to calibrate the equilibrium contact angle that the liquid forms with the solid walls and allows simulation of the flow of liquid and gas. This is at the cost of increased computational complexity, as the entire fluid is resolved, whereas in the above methods only the static interface shape is captured.

Mesoscopic models provide accurate solutions for complex 3D micro- and nano-scale structures. In general, one differentiates between lattice- and particle-based methods [20]. The lattice Boltzmann (LB) framework is a promising approach since it can capture complex boundary conditions such as rough surfaces [21] and is suitable for parallelization and GPU-accelerated computations [20,22,23]. It allows simulations in the continuum flow regime as well as in the slip flow regime [24].

The LB method is a popular method for which a wide range of models exist, capable of solving non-isothermal flow, evaporation [25], and multiphysics problems where several physical phenomena are coupled. This includes simulations of fluid–structure interactions, where the motion of a solid body affects the fluid flow [26,27].

In this work, an isothermal multiphase lattice Boltzmann (LB) method is used to model the liquid–gas interface. We applied a D3Q27 multiphase LB method with 27 discrete velocities ($\mathbf{c}_i$, $i = 0.26$) at every lattice point in a 3D space [28] to validate the theoretical findings. The LB method simulates the evolution of the discrete density distribution function $f_i(\mathbf{x}, t)$, which describes the probability of finding a particle at position $\mathbf{x}$ with velocity $\mathbf{c}_i$ at time t. The time evolution can be written as:

$$f_i(\mathbf{x}+\mathbf{c}_i\Delta t, t+\Delta t) - f_i(\mathbf{x}, t) = -\frac{1}{\tau}\left[f_i(\mathbf{x}, t) - f_i^{eq}(\rho, \mathbf{v}, \mathbf{x}, t)\right] \tag{11}$$

The term on the right is the Bhatnagar–Gross–Krook approximation of the collision operator, reflecting the inter-particle collisions in the fluid [29]. The relaxation time τ is linked to the viscosity of the fluid. In the LB method, the discrete one-body distribution function f_i is relaxed towards a local equilibrium f_i^{eq}. The term on the left represents the propagation of the density distribution function. In this step, the f_is are streamed to their respective neighbouring cells.

The LB method is usually not simulated with SI units but as a similarity problem. For our LB simulation, we used the common LB unit convention: the time step (ts) was set to one, the lattice spacing (Δx) was set to one lattice unit (lu), and the mass of one fluid particle (m) was set to one mass unit (mu). This way, the LB unit convention gave $\Delta t = 1$ ts, $\Delta x = 1$ lu, $m = 1$ mu. Therefore, the speed of sound equalled $c_s = 1/\sqrt{3}\,\mathrm{lu/ts}$ for the D3Q27 lattice. As is typically done for such multiphase LB simulations, e.g., in Peng et al. [30], for increased stability and faster numerical convergence we chose $\tau = 1$ ts for our simulations. This corresponds to a kinematic viscosity of $1/6\,\mathrm{lu}^2/\mathrm{ts}$ ($\nu = c_s^2(\tau - 0.5)\Delta t$).

The Bond number ($\mathrm{Bo} = \Delta\rho g L^2/\gamma$) describes the ratio of gravitational to capillary forces [31]: γ represents the surface tension, $\Delta\rho$ is the density difference between the liquid

and gaseous phases, g is the gravitational acceleration, and L is the characteristic length. In this paper, we focus exclusively on examples with Bo $\ll 1$ so that gravitational effects can be neglected.

The LB method is designed to reproduce the Navier–Stokes equation in the hydrodynamic limit [28]. Macroscopic quantities such as density and velocity can be calculated by summing up the discrete populations f_i and discrete velocities c_i [28].

$$\rho = \sum_{i=0}^{26} f_i \tag{12}$$

$$\mathbf{v} = \frac{1}{\rho} \sum_{i=0}^{26} f_i \mathbf{c}_i \tag{13}$$

In this case, the guided equilibrium (GE) model proposed in [28,32] was used. Further implementation details can be found in [18,28,32].

The Shan–Chen multiphase model was chosen [30,33,34]. The interaction between fluid particles was achieved by including the following force:

$$\mathbf{F} = -G\psi(\mathbf{x}, t) \sum_{i=0}^{26} w_i \psi(\mathbf{x} + \mathbf{c}_i \Delta t, t) \mathbf{c}_i \tag{14}$$

This leads to the non-ideal equation of state shown in Equation (15). The function $\psi(\rho)$ describes the interaction potential and depends on the density, whereas G describes the interaction strength between the fluid particles and allows the surface tension to be adjusted.

$$p(\rho) = \rho RT + \frac{GRT}{2} (\psi(\rho))^2 \tag{15}$$

For the interaction between the fluid and solid, the following force is introduced, with the function $s(\mathbf{x})$ giving 1 for solid nodes and 0 for fluid nodes [30,35].

$$\mathbf{F}_{ads} = -G_{ads} \psi(\mathbf{x}, t) \sum_{i=0}^{26} w_i s(\mathbf{x} + \mathbf{c}_i \Delta t, t) \mathbf{c}_i \tag{16}$$

The parameter G_{ads} correlates linearly with the contact angle α_0 for a given G value, as shown in the contact angle benchmark in [18]. G_{ads} allows tuning the contact angle of a liquid droplet on the flat solid phase. Therefore, with G_{ads} the hydrophobicity can be controlled. Implementation details on how the forces are incorporated into the LB method can be found in [18,30,33,34].

Additionally, a non-slip (bounce-back) boundary condition was employed for the fluid–solid interaction. Periodic boundary conditions (PBCs) were employed at the border of the domain. If not stated otherwise, PBCs were used in all directions, x, y, and z.

For the simulations in this work we used $G = 180.0$, which results in a surface tension of: $\gamma = 68.45\,\mathrm{mu\,ts^{-2}}$ in the LB unit convention. Further implementation details and validation benchmarks for the surface tension calculation can be found in [18]. Since the shape of the CMC surface depends only on the boundary conditions (three-phase contact line) and $q := \Delta p / \gamma\,[\mathrm{lu}^{-1}]$, it is sufficient to ensure that q and α_0 correspond to the real physical problem. Dimensionalization of the problem works as follows: $\Delta p^{SI} / \gamma^{SI} = q^{SI} = q / \Delta x^{SI}$. Here Δx^{SI} is the lattice spacing in SI units. The convergence criterium stated in Equation (17) was fulfilled with $\epsilon = 10^{-8}$ for all the simulations.

$$\epsilon \geq \max_{x,y,z} \left(\frac{|\rho^t(x,y,z) - \rho^{t-1}(x,y,z)|}{\rho^{t-1}(x,y,z)} \right) \tag{17}$$

For the simulations, a high-performance computing code was adapted [36]. The code uses a hybrid CUDA–MPI programming layout that enables it to be executed on several

NVIDIA GPUs in parallel. In the D3Q27 LB method, the evolution of a 27–distribution function has to be calculated at each lattice node. This includes three major steps: collision, streaming, and force calculation. Since the method is explicit and all calculations are local, multithread parallelization within the GPU can be employed efficiently.

All 3D figures in this work were created using ParaView [37], and all 2D figures were created using the Python package Matplotlib.

4. Results

4.1. Theoretical Analysis of the Constant Mean Curvature Surface for a Combined Pillar–Pore Structure

With Equation (10) and the the divergence in cylindrical coordinates (Equation (5)), the Young–Laplace equation can be expressed in cylindrical coordinates. The origin of the coordinate system is set in the centre of the pillar. In this work, we theoretically analysed the CMC problem only for the much simpler rotationally symmetric case. Therefore, the Young–Laplace equation simplifies to:

$$\operatorname{div} \hat{\mathbf{n}} = \frac{1}{r}\frac{\partial}{\partial r}\left(r\frac{\partial f(r)}{\partial r}\left(1+\left(\frac{\partial f(r)}{\partial r}\right)^2\right)^{-\frac{1}{2}}\right) = \frac{\Delta p}{\gamma} =: q \tag{18}$$

Rearranging and integration yields:

$$rf'(r)\left(1+f'(r)^2\right)^{-\frac{1}{2}} = \frac{1}{2}qr^2 + c_0 \qquad \text{with } c_0 \in \mathbb{R} \tag{19}$$

$$\Leftrightarrow rf'(r) = \left(\frac{1}{2}qr^2 + c_0\right)\left(1+f'(r)^2\right)^{\frac{1}{2}} \tag{20}$$

Finally, one can solve for $f'(r)$

$$f'_{+/-}(r) = \pm\sqrt{\frac{(0.5qr^2+c_0)^2}{r^2-(0.5qr^2+c_0)^2}} = \pm\frac{|0.5qr^2+c_0|}{\sqrt{r^2-(0.5qr^2+c_0)^2}} \tag{21}$$

and one finds two solutions for the original differential equation: $f'_-(r)$ represents a solution with negative slope and $f'_+(r)$ represents a solution with positive slope.

Assuming the extremum is at $r = R > r_p$, then $f'_{+/-}(r)|_{r=R} = 0$ provides the following expression for c_0:

$$c_0 = -0.5qR^2 \tag{22}$$

One can also derive a dimensionless form for $f'_{+/-}$:

$$f'_{+/-}\left(\frac{r}{R}, qR\right) = \pm\sqrt{\frac{\left(\left(\frac{r}{R}\right)^2-1\right)^2}{\frac{4}{(qR)^2}\left(\frac{r}{R}\right)^2-\left(\left(\frac{r}{R}\right)^2-1\right)^2}} \tag{23}$$

Solving Equation (21) for q gives:

$$q = \frac{2r\left|f'_{+/-}(r)\right|}{\sqrt{1+(f'_+(r))^2}|r^2-R^2|} > 0 \tag{24}$$

A geometrical expression for the slope of the function $f(r)$ in terms of α, the angle between the z-axis and $f(r)$, is given by Equation (25).

$$f'_{+/-}(r) = \pm\tan(\alpha - \frac{\pi}{2}) \qquad \text{with } \alpha \in [90°, 180°] \tag{25}$$

Solving Equation (21) for R, inserting Equation (25), and applying the trigonometric relation $\tan(x)/\sqrt{1+\tan^2(x)} = \sin(x)$, one can derive Equation (26).

$$R = \sqrt{r^2 - \frac{2rf'_{+/-}(r)}{q\sqrt{1+(f'_{+/-}(r))^2}}} = \sqrt{r^2 \pm \frac{2r\cos(\alpha)}{q}} \tag{26}$$

For a hydrophobic structure consisting of a cylindrical pore (radius r_c) with a pillar (radius r_p) in the centre (see Figures 3 and 4), the solution can be constructed with $f_-(r)$ for $r_p \leq r \leq R$ and $f_+(r)$ for $R < r \leq r_c$. To ensure continuity, $f'_-(r)|_{r=R} = f'_+(r)|_{r=R} = 0$ and $f_-(R) = f_+(R)$ have to be fulfilled; $f_-(r)$ and $f_+(r)$ both have their minimum at $r = R$ and share the same $c_0 = -0.5qR^2$. The expression for $f'(r)$ is then given by:

$$f'(r) = \frac{0.5qr^2 - 0.5qR^2}{\sqrt{r^2 - (0.5qr^2 - 0.5qR^2)^2}} \tag{27}$$

The integral of $f'(r)$ is an elliptic integral. The general form of an elliptic integral is given by the following equation according to [38]:

$$\int \frac{A(r)}{B(r)\sqrt{S(r)}}\mathrm{d}r \tag{28}$$

Here $A(r)$, $B(r)$ are polynomials in r and $S(r)$ is a polynomial of degree 3 or 4. For our case, it holds that $A(r) = 0.5qr^2 - 0.5qR^2$, $B(r) = 1$, and

$$S(r) = r^2 - (0.5qr^2 - 0.5qR^2)^2 \tag{29}$$

The roots of $S(r)$ are at $r_1 = (1+\sqrt{1+q^2R^2})/q$, $r_2 = (-1+\sqrt{1+q^2R^2})/q$, $r_3 = (1-\sqrt{1+q^2R^2})/q$, and $r_4 = (-1-\sqrt{1+q^2R^2})/q$ for $q \neq 0$.

The integral $\int f'(r)\mathrm{d}r$ has no expression in terms of elementary functions, since $S(r)$ has no repeated roots. With a reduction formula, every elliptic integral can be brought into a form that involves three elementary integrals (elliptic integrals of the first, second, and third kind) [38]. The software Mathematica [39] can calculate the reduction for our problem, and one finds that the solution depends on the elliptic integrals of the first and second kind. Nevertheless, the expression for $f'(r)$ can be used to derive some interesting properties. By a simple numerical integration, $f(r)$ can be determined:

$$f(r) = \int_{r_p}^{r} f'(\tilde{r})\mathrm{d}\tilde{r} + z_p = I(r) + z_p \tag{30}$$

An interesting family of solutions are those with identical contact angles at $r_p < R$ and $r_* > R$. This condition can be expressed by the following equation:

$$|f'(r)|_{r=r_p}| = |f'(r)|_{r=r_*}| \tag{31}$$

Solving for c_0 leads to

$$c_0 = -0.5qr_pr_* \tag{32}$$

Combining Equations (22) and (32) yields the following expression for the minimum's location:

$$R = \sqrt{r_pr_*} \tag{33}$$

This shows that the minimum's location for this specific case is independent of the contact angle.

Let α_p and α_c be the respective contact angles between the liquid and the pillar/pore wall. Combining Equation (26), evaluated at $r = r_p$, and Equation (33) gives:

$$R = \sqrt{r_p r_*} = \sqrt{r_p^2 - \frac{2r_p \cos(\alpha_p)}{q}} \tag{34}$$

$$\Rightarrow r_* = r_p - \frac{2\cos(\alpha_p)}{q} \tag{35}$$

Equipped with this solution, we can now derive an expression for the critical (liquid entry) pressure of a combined pillar–pore structure. For $q = 0$, the liquid–gas interface is flat. With increasing pressure, a torus-like meniscus starts to form (see Figure 3). The contact angles between liquid and pillar wall (α_p) and liquid and pore wall (α_c) begin to increase. In the beginning, water touches neither the pillar's lateral surface nor the pore wall. If the liquid does not wet the pillar and the pore wall it holds $|f'_+(r)|_{r=r_c}| < |f'_-(r)|_{r=r_p}|$, it follows that $\alpha_c < \alpha_p$. For a certain q_1, the equilibrium contact angle is reached at the pillar ($\alpha_p = \alpha_0$); the contact angle at the pore wall is, for this state, still smaller than the equilibrium contact angle ($\alpha_c < \alpha_0$). This state is plotted in Figure 4a; r_* is marked only as an aid line for visualisation purposes but is not part of the actual solution.

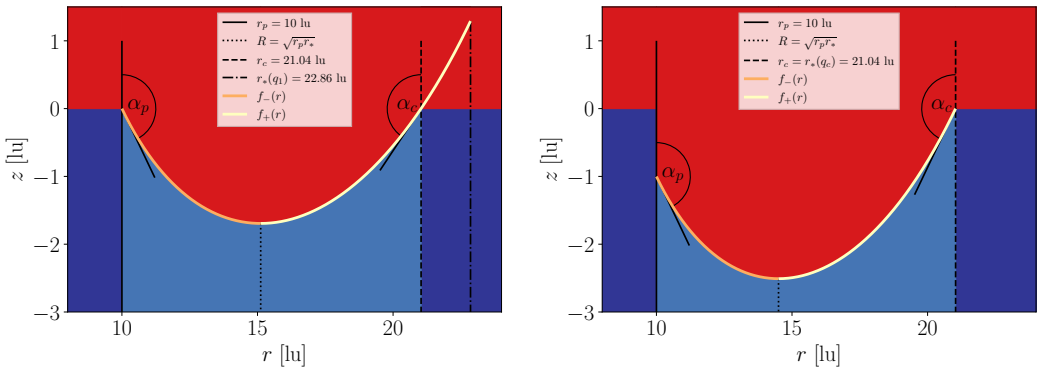

(**a**) (**b**)

Figure 4. Sketch of an intrusion of liquid into the pillar–pore structure. Solid is shown in dark blue, liquid in red, and gas in light blue, and the equilibrium contact angle is at $\alpha_0 = 130°$. Subfigure (**a**) shows a situation for $q_1 = 0.10\,\text{lu}^{-1}$, $\alpha_p = 130°$, and $\alpha_c < 130°$; r_* is solely marked as an aid line for visualisation purposes but is not part of the actual solution. Subfigure (**b**) shows the situation right before the break through with $q_{crit} = 0.12\,\text{lu}^{-1}$, $\alpha_p = 130°$, $\alpha_c = 130°$, and $r_* = r_c$; $f_-(r)$ and $f_+(r)$ form the liquid–gas interface. R is the location of the minimum, r_p is the pillar radius, and r_c is the pore radius.

As the pressure increases further and q exceeds q_1, liquid begins to slide down the pillar wall. As long as $\alpha_c < \alpha_0$, no water will wet the pore wall. While the liquid contact point at the pillar wall slides down, the contact angle at the pore wall increases and R shifts towards r_p. This process continues until the contact angle at the pore wall reaches the equilibrium contact angle ($\alpha_c = \alpha_p = \alpha_0$). At this point, $r_* = r_c$ (see Figure 4b), which, inserted in Equation (35), yields:

$$q_{crit} = \frac{-2\cos(\alpha_0)}{r_c - r_p} \tag{36}$$

In this critical state, a complete breakthrough occurs and the LEP (q_{crit}) is reached. Expressed in terms of Δp_{crit} and γ, one gets:

$$\Delta p_{crit} = \frac{-2\gamma \cos(\alpha_0)}{r_c - r_p} \tag{37}$$

The location of the minimum in the critical state is

$$R_{crit} = \sqrt{r_p r_c} \tag{38}$$

For $q \geq 2/(r_c - r_p)$, water will always intrude into the pillar–pore structure, independent of the hydrophobicity of the solid. In the limit of $r_p = 0$, we find the well-known equation for the LEP of a cylindrical pore (see Equation (2)).

Using the force-balance approach of Zheng et al. [19], one can directly derive the expression of the LEP, but without gaining any information about the shape of the liquid–gas interface.

$$F_z = \Delta p_{crit} \underbrace{(\pi r_c^2 - \pi r_p^2)}_{\substack{\text{cross sectional} \\ \text{area of pillar–} \\ \text{pore structure}}} + \gamma \underbrace{(2\pi r_p + 2\pi r_c)}_{\substack{\text{three-phase} \\ \text{contact line} \\ \text{length}}} \underbrace{\cos(\alpha_0)}_{\substack{\text{projection} \\ \text{along } z\text{-axis}}} = 0 \tag{39}$$

With the third binomial formula, one gets the following:

$$\Delta p_{crit} \pi (r_c - r_p)(r_c + r_p) = -2\gamma\pi \cos(\alpha_0)(r_p + r_c) \tag{40}$$

Simplification leads again to Equation (37).

One can also generalise this for the case where the pillar and the pore material have different equilibrium contact angles, α_0^p and α_0^c, respectively. In the critical state, it holds that at location r_p, $\alpha = \alpha_0^p$, and at location r_c, $\alpha = \alpha_0^c$. Combining these two conditions with Equation (26) gives:

$$\begin{aligned} R_{crit}^2 &= r_p^2 + \frac{2 r_p \cos(\alpha_0^p)}{q_{crit}} \\ &= r_c^2 - \frac{2 r_c \cos(\alpha_0^c)}{q_{crit}} \end{aligned} \tag{41}$$

Solving Equation (41) for q_{crit}, one can derive a generalised expression for the LEP of the pillar–pore structure:

$$q_{crit} = -2 \frac{r_p \cos(\alpha_0^p) + r_c \cos(\alpha_0^c)}{r_c^2 - r_p^2} \tag{42}$$

Inserting Equation (42) into Equation (26) with $r = r_p$ and $\alpha = \alpha_0^p$, one can derive a generalised form for R in the critical state.

$$\begin{aligned} R_{crit} &= \sqrt{r_p^2 + \frac{r_p \cos(\alpha_0^p)(r_c^2 - r_p^2)}{r_p \cos(\alpha_0^p) + r_c \cos(\alpha_0^c)}} \\ &= \sqrt{\frac{r_p r_c (r_c \cos(\alpha_0^p) + r_p \cos(\alpha_0^c))}{r_p \cos(\alpha_0^p) + r_c \cos(\alpha_0^c)}} \end{aligned} \tag{43}$$

The location of the minimum in the critical state depends on the two equilibrium contact angles. For the special case $\alpha_0^p = \alpha_0^c = \alpha_0$, the cosines cancel out and one finds again Equation (38). Combining R_{crit} and q_{crit} gives:

$$c_{0,crit} = -0.5 q_{crit} R_{crit}^2 = \frac{r_p r_c (r_c \cos(\alpha_0^p) + r_p \cos(\alpha_0^c))}{r_c^2 - r_p^2} \tag{44}$$

4.2. Numerical Calculation of the Constant Mean Curvature Surface and the Liquid Entry Pressure with the Lattice Boltzmann Method

4.2.1. Single Circular Pillar with Periodic Boundary Conditions

As a validation benchmark, we simulated a single pillar with periodic boundary conditions in the x- and y-directions and a closed boundary in the z-direction. At $z = 0$ lu, the domain boundary was closed with a slice of solid voxels, as well as on the opposite side of the domain at $z = 149$ lu. The total domain size was $200 \times 200 \times 150$ lu^3 (see Figure 5). These boundary conditions mimic a domain with periodically repeated pillars, as shown in Figure 2. The domain was initialized partly with water density and partly with gas density. Initially, the water was already surrounding part of the pillar and filled the entire upper part above the pillar. The simulation was then run until a static equilibrium state was reached. For the equilibrium state, the contact angle around the pillar was equal to the equilibrium contact angle and therefore the pressure difference between liquid and gas corresponded to the critical pressure calculated with Equation (3) from Zheng et al. [19].

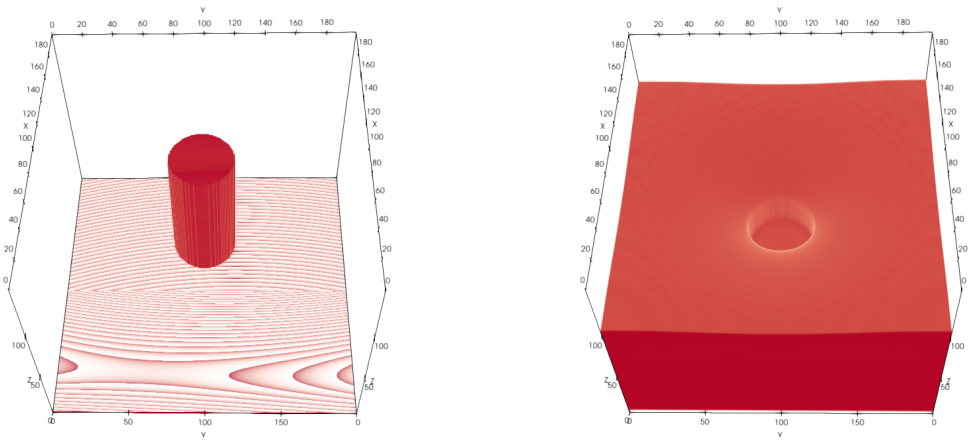

(**a**) (**b**)

Figure 5. (**a**) Solid domain structure with a single round pillar with PBC in x- and y-directions and a closed boundary in z-direction. At $z = 0$ lu, the domain boundary was closed with a slice of solid voxels, as well as on the other side of the domain at $z = 149$ lu. Boundary at $z = 149$ lu is not shown for better visibility. (**b**) Example of the density field after convergence of the multiphase LB simulation. Equilibrium state of the liquid (in red) for $r_p = 20$ lu and $\alpha_0 = 156.61°$. Gas and solid are not shown for better visibility.

As can be seen in Figure 6, we found that our LB simulations produced results which were in good agreement with the predictions from Equation (45) from Zheng et al. [19].

$$q_{crit}^{Zheng} = \frac{\Delta p_{crit}}{\gamma} = -\frac{2\pi r_p \cos(\alpha_0)}{P^2 - \pi r_p^2} \tag{45}$$

The value of q_{crit} from the LB simulation in Figure 6 was calculated with the equation of state (15) and $q_{crit} = (\overline{p(\rho_l)} - \overline{p(\rho_g)})/\gamma$. Here ρ_l is the density field of the liquid phase and ρ_g is the density field of the gas phase from the LB simulations; $\overline{p(\rho_l)}$ and $\overline{p(\rho_g)}$ represent the mean values of the liquid and gas pressure fields, respectively. This pressure

variation across the same phase emerges from the spurious velocities at the interface typical for this class of models. To reduce this effect, pressure values close to the interface were omitted. For more information on spurious currents, see Section 5. The errors for q_{crit} in Figure 6 are based on the standard deviation of the pressure field within each phase.

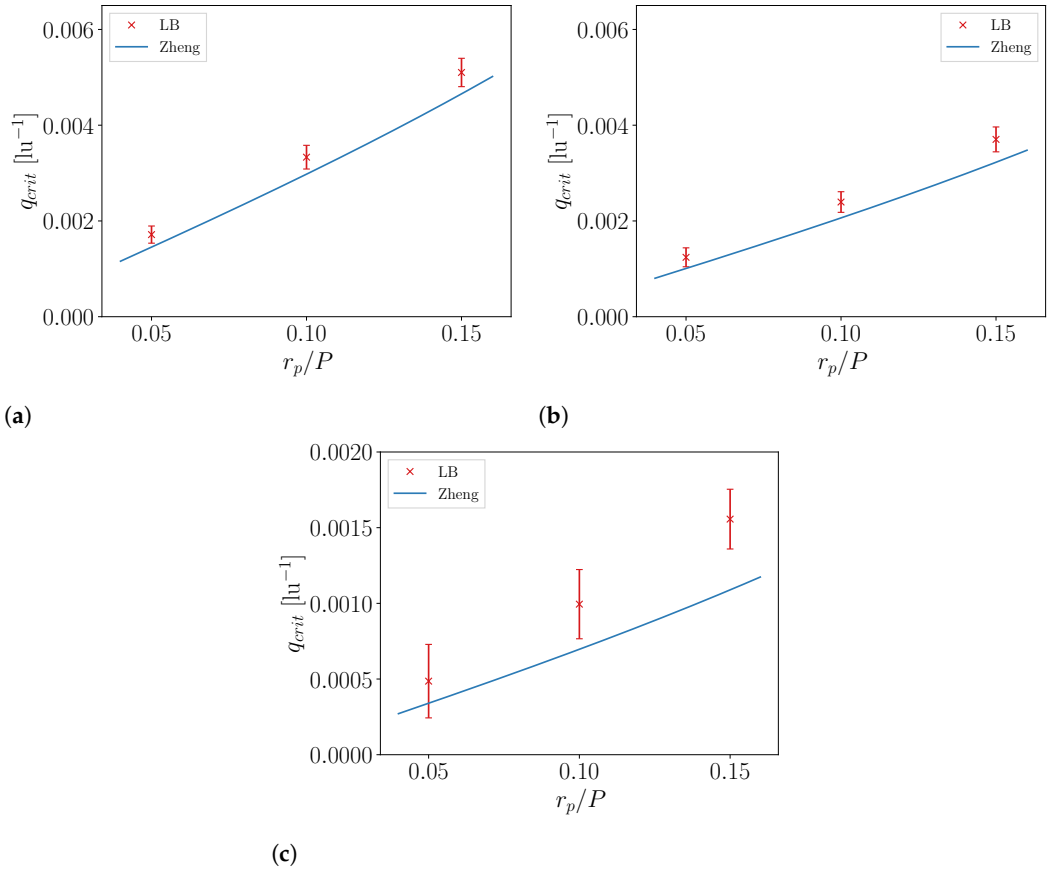

Figure 6. Values of q_{crit} for three different equilibrium contact angles and three different r_p values with $P = 200$ lu. Comparison between the LB results and Equation (45) from Zheng et al. [19]. In (**a**), $\alpha_0 = 156.61°$; in (**b**), $\alpha_0 = 129.51°$, and in (**c**), $\alpha_0 = 102.40°$.

4.2.2. Combined Pillar–Pore Structure

To validate our findings in Section 4.1, we ran 3D LB simulations. The upper boundary of the domain at $z = 0$ lu as well as the lower boundary at $z = 149$ lu were closed with a slice of solid voxels. In the centre we placed a cylindrical pore with radius $r_c = 99$ lu and a cylindrical pillar with radius $r_p = 20$ lu. The heights of the pillar and the pore were $h = 90$ lu. Above and below the pillar–pore structure was void space (see Figure 7). The total domain size was $200 \times 200 \times 150$ lu^3. For the simulations, the pillar and pore material had identical surface properties and therefore had the same equilibrium contact angle.

The domain was initialized partly with water density and partly with gas density. Initially, the water already filled part of the pillar–pore space and the entire upper part above the pillar–pore structure. The simulation was then run until a static equilibrium state was reached.

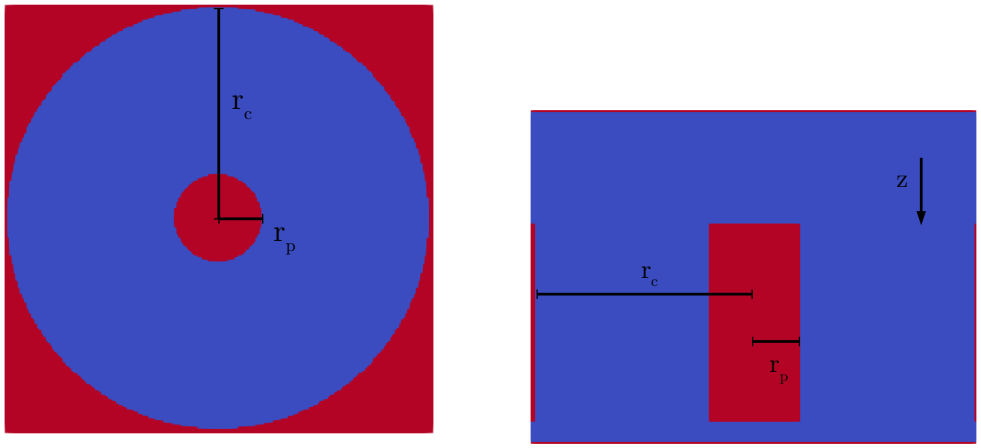

(**a**) (**b**)

Figure 7. Geometry of the combined pillar–pore structure: (**a**) top view and (**b**) side view. Solid is in red and void space in blue.

In an equilibrium state, the contact angles at the pillar wall and the pore wall will reach the equilibrium contact angle α_0. This is analogous to a droplet on a flat surface, for which the contact angle also becomes the equilibrium contact angle α_0 for the static state. The pressure difference will exactly be the critical pressure difference predicted by Equation (36) (see Figure 8).

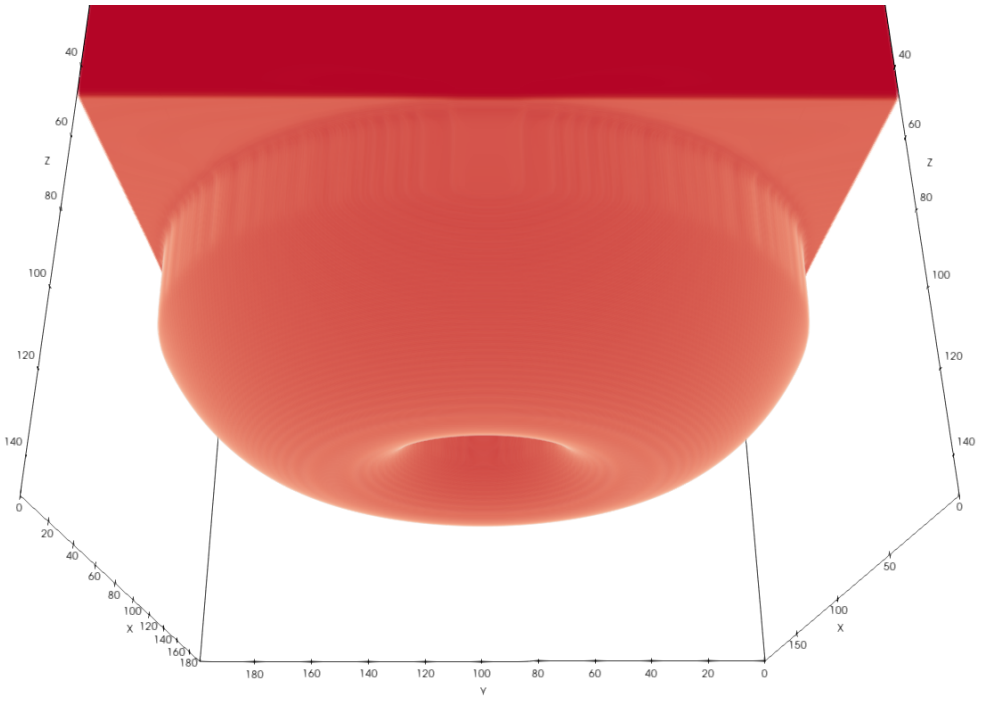

Figure 8. Liquid–gas interface within a combined pillar–pore structure. Example of the density field after convergence of the multiphase LB simulation for $\alpha_0 = 156.61°$, $r_p = 20$ lu, $r_c = 99$ lu, and a domain size of $200 \times 200 \times 150$ lu^3. Liquid is in red; gas and solid are not shown for better visibility.

Based on α_0, pill radius $r_p = 20$ lu, and pore radius $r_* = r_c = 99$ lu, we used Equation (36) to compute q_{crit} analytically and compared it to the LB simulation results (see Table 1); q_{crit}^{LB} from the LB simulation was again calculated with $q_{crit} = (\overline{p(\rho_l)} - \overline{p(\rho_g)})/\gamma$. The results are displayed in Table 1.

Table 1. Comparison between the LB simulation results and Equation (36). Respective q_{crit} values for $r_p = 20$ lu, $r_c = 99$ lu, and three different equilibrium contact angles. The error in parentheses was calculated based on the standard deviation of the pressure field within each phase. The last row shows the absolute deviation between LB simulation and theory.

G_{ads}	-80.0	-180.0	-280.0
α_0 (°)	156.61	129.51	102.40
q_{crit}^{LB} (lu^{-1})	0.02461	0.01781	0.00762
	(0.00042)	(0.00047)	(0.00035)
Equation (36) q_{crit} (lu^{-1})	0.02324	0.01610	0.00544
deviation (lu^{-1})	0.00137	0.00171	0.00218

To compare the shape of the interfaces with the LB simulation results, we numerically integrated Equation (27) with $c_0 = -0.5qr_pr_c$ and $q = q_{crit}^{LB}$ to obtain $f(r)$. These results are plotted together with the LB simulation results in Figure 9. For the numerical integration, we used the cumulative trapezoid method from the python3 package scipy (version 1.9.1) [40] with 1×10^4 points.

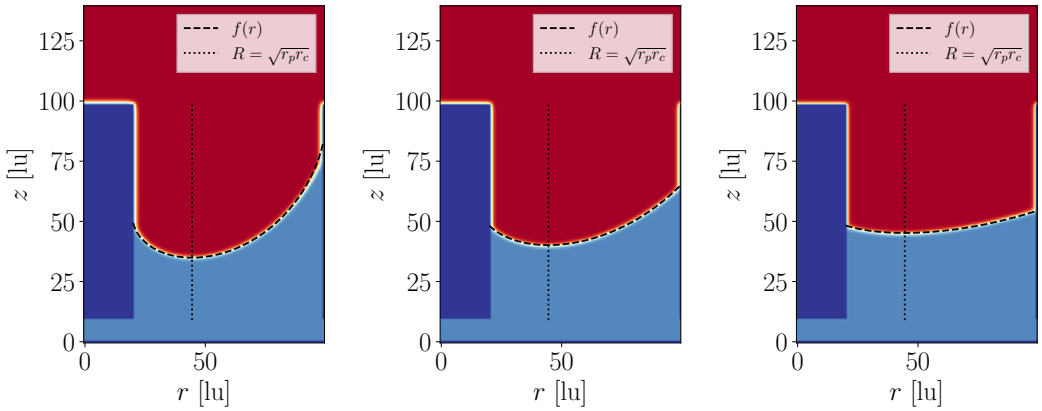

(**a**) (**b**) (**c**)

Figure 9. Shape of the liquid–gas interface for three different equilibrium contact angles. For a pillar radius of $r_p = 20$ lu and a pore radius of $r_c = 99$ lu. Cross-sections through $x = 99$ lu of the 3D density field from the multiphase LB simulation. The liquid is visualized in red, the gas in light blue, and the solid in dark blue; $f(r)$ shows the results based on the integral of Equation (27). In (**a**), $\alpha_0 = 156.61°$, in (**b**), $\alpha_0 = 129.51°$, and in (**c**), $\alpha_0 = 102.40°$.

To quantify the difference in the interface shape between the LB simulation and $f(r)$ from Equation (30), we calculated the normalised root mean square deviation (NRMSD) given in Equation (46). The lattice points right next to the solid walls were omitted because the boundary condition disturbs the density field close to the walls.

$$\mathrm{NRMSD} = \frac{100\,\%}{z_{max} - z_{min}} \times \sqrt{\frac{\sum_{j=r_p+2}^{r_c-2} [z_{IF,LB}(j) - f(j)]^2}{r_c - r_p - 3}} \tag{46}$$

First, we extracted the location of the liquid–gas interface (IF) from the LB simulation results. Based on the two-dimensional slice of the density field ($\rho_{j,k}$) shown in Figure 9 and the linear interpolation given in Equation (47), we were able to calculate the z positions of the liquid–gas interface from the LB simulations ($z_{IF,LB}$).

$$z_{IF,LB}(j) = k + \frac{\rho_c - \rho_{j,k}}{\rho_{j,k+1} - \rho_{j,k}} \qquad \text{with} \qquad \rho_{j,k} < \rho_c < \rho_{j,k+1} \tag{47}$$

Here $\rho_c = 0.5 \times (\rho_l + \rho_g)$ describes a critical density that defines the liquid–gas interface, $j \in [0, 1, \ldots, 99]$ is the position on the lattice in the r-direction, and $k \in [0, 1, \ldots, 149]$ is the position on the lattice in the z-direction.

$$z_p = \frac{\sum_{j=r_p+2}^{r_c-2} [z_{IF,LB}(j) - I(j)]}{r_c - r_p - 3} \tag{48}$$

The integral $I(r)$ in Equation (30) can be solved numerically, but $z_p = f(r_p)$ must also be determinant. To compute z_p, we used Equation (48), which minimizes the NRMSD in Equation (46). The results are shown in Figure 10.

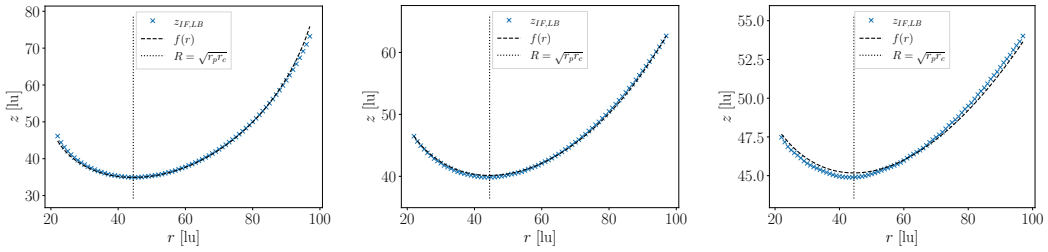

(**a**) (**b**) (**c**)

Figure 10. Shape of the liquid–gas interface for three different equilibrium contact angles: $f(r)$ shows the results based on the integral of Equation (27), and $z_{IF,LB}$ is the position of the interface predicted by the LB simulation. In (**a**), $\alpha_0 = 156.61°$, NRMSD = 1.53 %; in (**b**), $\alpha_0 = 129.51°$, NRMSD = 0.98 %, and in (**c**), $\alpha_0 = 102.40°$, NRMSD = 2.76 %.

5. Discussion

In this paper, we have derived an analytical expression for the liquid entry pressure of a combined pillar–pore structure and found good agreement with the predictions of the LB method. In all cases, the predictions for q_{crit} by the LB simulations were larger than the values predicted by the analytical analysis (see Table 1 and Figure 6). The largest deviation for q_{crit} was found for the smallest equilibrium contact angle ($\alpha_0 = 102.40°$; see Table 1). We identified three main sources of error. One error originates from the numerical limitations of the multiphase LB simulation, which was estimated by the standard deviation of the pressure field within each phase. This error in the pressure field originates from the spurious currents close to the interface that are typical for pseudo potential multiphase models [41]. This error could be minimized by an improved LB multiphase model and/or a higher resolution, which increases the computational cost of the simulation. Possible improvements are multi relaxation time [42] or entropic [43] LB models. A detailed discussion of contact angles in the pseudo-potential lattice Boltzmann modelling can be found in [17]. Changing model parameters such as the G parameter could also lead to smaller spurious currents and reduce the perturbation in the pressure field. However, this can only partially explain the deviation between the values of q_{crit} reported in Table 1. Other sources of error are the equilibrium contact angle calculations and the surface tension calculations based on benchmarks to calibrate the model. These systematic errors explain why we found consistently higher values in Table 1 and Figure 6 for the LB results compared to the theory. Moreover, the $\cos(\alpha_0)$ dependence of q_{crit} (see, e.g., Equation (36)) explains why the biggest error was found for the smallest equilibrium contact angle in Table 1. The equilibrium contact angle calculation can have an uncertainty of several degrees, and for values close to 90°, this error is amplified much more since the cosine has its largest derivative at 90°. Error propagation gives $\Delta q_{crit} = |2\sin(\alpha_0)/(r_c - r_p)|\Delta\alpha_0$. For more information on the equilibrium contact angle and surface tension calculations for the LB simulation results, see [18]. The shape of the interface and the location of the minimum calculated with Equations (30) and (38), respectively, agree very well with the predictions of the LB simulation. The NRMSD of the interface shape lies, for all three test cases, below

3 %, where the largest deviation was found, again, for the smallest equilibrium contact angle (See Figures 9 and 10).

In this paper, we only considered the case for which the cylindrical pore and the pillar have the same height. However, the reasoning in Section 4.1 can be applied in a similar way to a structure for which the pillar height exceeds or falls below that of the pore height, so that Equation (42) is universally applicable to any hydrophobic rotationally symmetric pillar–pore structure. Moreover the presented pillar–pore structure case can serve as a benchmark for the development and validation of numerical multiphase models.

Author Contributions: Conceptualization, T.J.; methodology, T.J., N.I.P. and S.L.; software, T.J. and N.I.P.; validation, T.J., J.K., N.I.P. and S.L.; formal analysis, T.J.; investigation, T.J., J.K., N.I.P. and S.L.; resources, N.I.P. and S.L.; data curation, T.J.; writing—original draft preparation, T.J.; writing—review and editing, T.J., J.K., N.I.P. and S.L.; visualization, T.J. and J.K.; supervision, N.I.P. and S.L.; project administration, T.J., N.I.P. and S.L.; funding acquisition, N.I.P. and S.L. All authors have read and agreed to the published version of the manuscript.

Funding: University of Luxembourg, Paul Scherrer Institute.

Informed Consent Statement: Not applicable.

Data Availability Statement: Simulation results from Section 4.2 are available at the following links: https://doi.org/10.6084/m9.figshare.22574173, https://doi.org/10.6084/m9.figshare.22574176.

Acknowledgments: We are thankful for the many fruitful discussions with Filip Janasz. The calculations in this paper were carried out using the HPC facilities of the University of Luxembourg [44] (see `hpc.uni.lu`) and the Swiss Supercomputing Center CSCS (project s1155). We also thank the University of Luxembourg and SwissNuclear for their support.

Conflicts of Interest: The authors declare no conflicts of interest.

Abbreviations

CMC	Constant mean curvature
PDE	Partial differential equation
Δp_{crit}	Liquid entry pressure (LEP)
γ	Surface tension
q	$\Delta p/\gamma$
r_p	Pillar radius
r_c	Pore radius
R	Location of the minimum
α_p	Contact angles between the liquid and the pillar wall
α_c	Contact angles between the liquid and the pore wall
α_0	Equilibrium contact angle between liquid and solid
P	Pitch pillar (periodicity in x- and y-directions)
A_c	Area of the periodically repeated cell ($A_c = P \times P$)
A	Top area of the pillar ($A = \pi r_p^2$)
l	Perimeter of the pillar ($l = 2\pi r_p$)
$\hat{\mathbf{n}}$	Unit normal vector of the liquid–gas interface
LB	lattice Boltzmann
NRMSD	normalised root mean square deviation
p	Pressure
ρ	Density
ρ_l	Liquid density
ρ_g	Gas density
$\mathbf{F}$	Force
Δx	Lattice spacing
Δt	Time step
m	Fluid particle mass

G_{ads}	LB parameter to tune the equilibrium contact angle
G	LB parameter to control the fluid–fluid interaction strength
τ	Relaxation time
ν	Kinematic viscosity
c_s	Speed of sound
g	Gravitation acceleration
$\mathbf{v}$	Velocity
$\mathbf{c_i}$	Discrete lattice velocity

References

1. Jung, Y.; Bhushan, B. Wetting behaviour during evaporation and condensation of water microdroplets on superhydrophobic patterned surfaces. *J. Microsc.* **2008**, *229*, 127–140. [CrossRef] [PubMed]
2. Gogolides, E.; Ellinas, K.; Tserepi, A. Hierarchical micro and nano structured, hydrophilic, superhydrophobic and superoleophobic surfaces incorporated in microfluidics, microarrays and lab on chip microsystems. *Microelectron. Eng.* **2015**, *132*, 135–155. [CrossRef]
3. Xiao, Z.; Zheng, R.; Liu, Y.; He, H.; Yuan, X.; Ji, Y.; Li, D.; Yin, H.; Zhang, Y.; Li, X.M.; et al. Slippery for scaling resistance in membrane distillation: A novel porous micropillared superhydrophobic surface. *Water Res.* **2019**, *155*, 152–161. [CrossRef] [PubMed]
4. Agonafer, D.D.; Lee, H.; Vasquez, P.A.; Won, Y.; Jung, K.W.; Lingamneni, S.; Ma, B.; Shan, L.; Shuai, S.; Du, Z.; et al. Porous micropillar structures for retaining low surface tension liquids. *J. Colloid Interface Sci.* **2018**, *514*, 316–327. [CrossRef]
5. Yao, X.; Gao, J.; Song, Y.; Jiang, L. Superoleophobic Surfaces with Controllable Oil Adhesion and Their Application in Oil Transportation. *Adv. Funct. Mater.* **2011**, *21*, 4270–4276. [CrossRef]
6. Xue, Z.; Wang, S.; Lin, L.; Chen, L.; Liu, M.; Feng, L.; Jiang, L. A Novel Superhydrophilic and Underwater Superoleophobic Hydrogel-Coated Mesh for Oil/Water Separation. *Adv. Mater.* **2011**, *23*, 4270–4273. [CrossRef] [PubMed]
7. Field, R.W. Separation by reconfiguration. *Nature* **2012**, *489*, 41–42. [CrossRef]
8. Sridhar, A.; Ong, C.L.; Paredes, S.; MicheL, B. Thermal Design of a Hierarchical Radially Expanding Cavity for Two-Phase Cooling of Integrated Circuits. In Proceedings of the International Electronic Packaging Technical Conference and Exhibition, Changsha, China, 11–14 August 2015; Volume 1. [CrossRef]
9. Kim, B.S.; Harriott, P. Critical entry pressure for liquids in hydrophobic membranes. *J. Colloid Interface Sci.* **1987**, *115*, 1–8. [CrossRef]
10. Rahimpour, M.R.; Esmaeilbeig, M.A. Chapter 6—Membrane Wetting in Membrane Distillation. In *Current Trends and Future Developments on (Bio-) Membranes*; Basile, A., Curcio, E., Inamuddin, Eds.; Elsevier: Amsterdam, The Netherlands, 2019; pp. 143–174. [CrossRef]
11. Lobaton, E.; Salamon, T. Computation of constant mean curvature surfaces: Application to the gas–liquid interface of a pressurized fluid on a superhydrophobic surface. *J. Colloid Interface Sci.* **2007**, *314*, 184–198. [CrossRef]
12. Laplace, P.S. Supplément au dixième livre du Traité de Mécanique Céleste. *J.B.M. Duprat* **1805**, *4*, 1–79.
13. Racz, G.; Kerker, S.; Kovács, Z.; Vatai, G.; Ebrahimi, M.; Czermak, P. Theoretical and Experimental Approaches of Liquid Entry Pressure Determination in Membrane Distillation Processes. *Period. Polytech. Chem. Eng.* **2014**, *58*, 81–91. [CrossRef]
14. Young, T. III. An essay on the cohesion of fluids. *Philos. Trans. R. Soc. Lond.* **1805**, *95*, 65–87. [CrossRef]
15. Kwok, D.; Neumann, A. Contact angle measurement and contact angle interpretation. *Adv. Colloid Interface Sci.* **1999**, *81*, 167–249. [CrossRef]
16. Ruiz-Cabello, F.J.M.; Rodríguez-Valverde, M.A.; Marmur, A.; Cabrerizo-Vílchez, M.A. Comparison of Sessile Drop and Captive Bubble Methods on Rough Homogeneous Surfaces: A Numerical Study. *Langmuir* **2011**, *27*, 9638–9643. [CrossRef] [PubMed]
17. Li, Q.; Luo, K.H.; Kang, Q.J.; Chen, Q. Contact angles in the pseudopotential lattice Boltzmann modeling of wetting. *Phys. Rev. E Stat. Nonlin. Soft Matter. Phys.* **2014**, *90*, 053301. [CrossRef] [PubMed]
18. Jäger, T.; Mokos, A.; Prasianakis, N.I.; Leyer, S. Pore-Level Multiphase Simulations of Realistic Distillation Membranes for Water Desalination. *Membranes* **2022**, *12*, 1112. [CrossRef]
19. Zheng, Q.S.; Yu, Y.; Zhao, Z.H. Effects of hydraulic pressure on the stability and transition of wetting modes of superhydrophobic surfaces. *Langmuir* **2005**, *21*, 12207–12212. [CrossRef]
20. Schiller, U.D.; Krüger, T.; Henrich, O. Mesoscopic modelling and simulation of soft matter. *Soft Matter* **2018**, *14*, 9–26. [CrossRef]
21. Xiong, W.; Cheng, P. Mesoscale simulation of a molten droplet impacting and solidifying on a cold rough substrate. *Int. Commun. Heat Mass Transf.* **2018**, *98*, 248–257. [CrossRef]
22. Prasianakis, N.I.; Rosén, T.; Kang, J.; Eller, J.; Mantzaras, J.; Büichi, F.N. Simulation of 3D Porous Media Flows with Application to Polymer Electrolyte Fuel Cells. *Commun. Comput. Phys.* **2013**, *13*, 851–866. [CrossRef]
23. Rosen, T.; Eller, J.; Kang, J.; Prasianakis, N.I.; Mantzaras, J.; Büchi, F.N. Saturation dependent effective transport properties of PEFC gas diffusion layers. *J. Electrochem. Soc.* **2012**, *159*, F536. [CrossRef]
24. Luo, K.; Xia, J.; Monaco, E. Multiscale modelling of multiphase flow with complex interactions. *J. Multiscale Model.* **2009**, *1*, 125–156. [CrossRef]

25. Qin, F.; Del Carro, L.; Mazloomi Moqaddam, A.; Kang, Q.; Brunschwiler, T.; Derome, D.; Carmeliet, J. Study of non-isothermal liquid evaporation in synthetic micro-pore structures with hybrid lattice Boltzmann model. *J. Fluid Mech.* **2019**, *866*, 33–60. [CrossRef]
26. Afra, B.; Amiri Delouei, A.; Mostafavi, M.; Tarokh, A. Fluid-structure interaction for the flexible filament's propulsion hanging in the free stream. *J. Mol. Liq.* **2021**, *323*, 114941. [CrossRef]
27. Afra, B.; Karimnejad, S.; Amiri Delouei, A.; Tarokh, A. Flow control of two tandem cylinders by a highly flexible filament: Lattice spring IB-LBM. *Ocean Eng.* **2022**, *250*, 111025. [CrossRef]
28. Prasianakis, N.I.; Karlin, I.V.; Mantzaras, J.; Boulouchos, K.B. Lattice Boltzmann method with restored Galilean invariance. *Phys. Rev. E* **2009**, *79*, 066702. [CrossRef]
29. Qian, Y.H.; D'Humières, D.; Lallemand, P. Lattice BGK Models for Navier-Stokes Equation. *Europhys. Lett. (EPL)* **1992**, *17*, 479–484. [CrossRef]
30. Peng, C.; Tian, S.; Li, G.; Sukop, M.C. Single-component multiphase lattice Boltzmann simulation of free bubble and crevice heterogeneous cavitation nucleation. *Phys. Rev. E* **2018**, *98*, 023305. [CrossRef]
31. Kunes, J. *Dimensionless Physical Quantities in Science and Engineering*; Elsevier Scientific Pub. Co.: Amsterdam, The Netherlands; New York, NY, USA, 2012.
32. Safi, M.A.; Mantzaras, J.; Prasianakis, N.I.; Lamibrac, A.; Büchi, F.N. A pore-level direct numerical investigation of water evaporation characteristics under air and hydrogen in the gas diffusion layers of polymer electrolyte fuel cells. *Int. J. Heat Mass Transf.* **2019**, *129*, 1250–1262. [CrossRef]
33. Shan, X.; Chen, H. Lattice Boltzmann model for simulating flows with multiple phases and components. *Phys. Rev. E* **1993**, *47*, 1815–1819. [CrossRef]
34. Shan, X.; Chen, H. Simulation of nonideal gases and liquid-gas phase transitions by the lattice Boltzmann equation. *Phys. Rev. E* **1994**, *49*, 2941. [CrossRef] [PubMed]
35. Sukop, M.C.; Thorne, D.T. *Lattice Boltzmann Modeling*; Springer: Berlin/Heidelberg, Germany, 2006.
36. Safi, M.A.; Prasianakis, N.I.; Mantzaras, J.; Lamibrac, A.; Büchi, F.N. Experimental and pore-level numerical investigation of water evaporation in gas diffusion layers of polymer electrolyte fuel cells. *Int. J. Heat Mass Transf.* **2017**, *115*, 238–249. [CrossRef]
37. Ahrens, J.; Geveci, B.; Law, C. ParaView: An End-User Tool for Large Data Visualization. In *Visualization Handbook*; Elesvier: Amsterdam, The Netherlands, 2005; ISBN 978-0123875822.
38. Weisstein, E.W. Elliptic Integral. From MathWorld—A Wolfram Web Resource. 2023. Available online: https://mathworld.wolfram.com/EllipticIntegral.html (accessed on 9 March 2023).
39. Wolfram Inc. *Mathematica, Version 13.2*; Wolfram Inc.: Champaign, IL, USA, 2022.
40. Virtanen, P.; Gommers, R.; Oliphant, T.E.; Haberland, M.; Reddy, T.; Cournapeau, D.; Burovski, E.; Peterson, P.; Weckesser, W.; Bright, J.; et al. SciPy 1.0: Fundamental Algorithms for Scientific Computing in Python. *Nat. Methods* **2020**, *17*, 261–272. [CrossRef]
41. Chen, L.; Kang, Q.; Mu, Y.; He, Y.L.; Tao, W.Q. A critical review of the pseudopotential multiphase lattice Boltzmann model: Methods and applications. *Int. J. Heat Mass Transf.* **2014**, *76*, 210–236. [CrossRef]
42. Peng, H.; Zhang, J.; He, X.; Wang, Y. Thermal pseudo-potential lattice Boltzmann method for simulating cavitation bubbles collapse near a rigid boundary. *Comput. Fluids* **2021**, *217*, 104817. [CrossRef]
43. Mazloomi M., A.; Chikatamarla, S.S.; Karlin, I.V. Entropic lattice Boltzmann method for multiphase flows: Fluid-solid interfaces. *Phys. Rev. E* **2015**, *92*, 023308. [CrossRef] [PubMed]
44. Varrette, S.; Cartiaux, H.; Peter, S.; Kieffer, E.; Valette, T.; Olloh, A. Management of an Academic HPC & Research Computing Facility: The ULHPC Experience 2.0. In Proceedings of the 6th ACM High Performance Computing and Cluster Technologies Conference (HPCCT 2022), Fuzhou, China, 8–10 July 2022; Association for Computing Machinery (ACM): Fuzhou, China, 2022.